Microchimica Acta (2021) 188: 95
https://doi.org/10.1007/s00604-021-04755-8

ORIGINAL PAPER

A covalent organic polymer–TiO_2/Ti_3C_2 heterostructure as nonenzymatic biosensor for voltammetric detection of dopamine and uric acid

Xing Lu[1] · Songnan Li[2] · Wei Guo[1] · Feng Zhang[1] · Fengyu Qu[1]

Received: 4 December 2020 / Accepted: 15 February 2021 / Published online: 22 February 2021

Abstract

Heterostructures have potential to blend the advantages of each material, even exhibiting the evolutionary performance due to synergistic effects. Herein, covalent organic polymers (NUF) are integrated with a $TiO_2/Ti_3C_2T_x$ nanocomposite (TiO_2/TiCT) to form TiO_2/TiCT-NUF heterojunctions as an enlarged nonenzymatic biosensor for dopamine (DA) and uric acid (UA). Detection is performed by differential pulse voltammetry (DPV). The TiO_2/TiCT/NUF exhibits high sensing activity with low detection limits of 0.2 and 0.18 nM ($S/N = 3$) in the concentration ranges from 0.002 to 100 μM and 0.001 to 60 μM for simultaneous determination of DA and UA, respectively. In addition, the TiO_2/TiCT/NUF provides good selectivity and reproducibility for DA and UA detection in urine and serum samples with recoveries of 98.4 to 100.9%. The proposed heterojunctions manifest an intriguing potential as a candidate of an electrochemical sensor for sole and simultaneous detection of DA and UA.

Keywords Heterostructures · Covalent organic polymers · TiO_2/Ti_3C_2 biosensor · Dopamine · Uric acid

Introduction

Physiological fluids embrace biomolecules such as dopamine (DA) and uric acid (UA), capable of regulating life functions [1]. Concretely, DA participates in reconciling the function of nervous system [2], and UA is generally reckoned as the termination product of purine circulation [3]. The deviant level of DA and UA in bodily fluids would trigger certain disorders and diseases, such as Parkinsonism, schizophrenia, and gout, renal disease [4], respectively. Consequently, it is paramount to quickly and accurately distinguish DA and UA in fluids. Preferably, comparison to other apparatus mediums that require specialized large instruments [5–7], an electroanalytical technique is a highly striking method in monitoring DA and UA [8]. Also, various materials have acquired an appreciable focus for the sole or synchronous detection of DA and UA [9], but each has its typical impediments. This originates from the structural similarities of DA and UA, which lead to their oxidation potentials so similar that is difficult to distinguish their voltammetric peaks [10], and coexistence of species in biofluids may result in serious disturbance on the detection of DA and UA (i.e., serum, urine) [11]. Thus, it is of emerging concern to exploit new materials for the electrochemical detection of DA and UA.

A branch of promising porous materials, covalent organic polymers (COPs) assembling by strong covalent bonds with light elements (C, N, O, and B) [12], have been applied in gas storage/separation [13], photocatalytic [14], and electrocatalysis [15]. Presently, only several COP-based sensing platforms are developed to detect targets by predicating on colorimetric [16], fluorescent feedbacks [17], instead of electrochemical ones due to their intrinsically weak electrical conductivity and low dispensability [18]. One strategy is to support/combine COPs with conductive matrixes materials [19, 20]. In this regard, a two-dimensional titanium carbide ($Ti_3C_2T_x$) is a sane support due to its graphene-like peculiarity with metallic, hydrophilic, and electroactive surface [21]. Interestingly, the partially oxidized $Ti_3C_2T_x$ MXene (TiO_2/

✉ Feng Zhang
zhangfeng@hrbnu.edu.cn

✉ Fengyu Qu
qufengyu@hrbnu.edu.cn

[1] Key Laboratory of Photochemical Biomaterials and Energy Storage Materials, Heilongjiang Province and College of Chemistry and Chemical Engineering, Harbin Normal University, Harbin 150025, People's Republic of China

[2] Modern Experiment Center, Harbin Normal University, Harbin 150025, People's Republic of China

Ti_3C_2) is conducive to enhancing the number of carriers [22], resulting in more electrons to participate in redox reaction [23]. To our survey, there remains in a budding stage on COPs for DA and UA detection, and the sparse examples are employed COPs to combine with TiO_2/Ti_3C_2 nanohybrid as electrochemical sensors.

Impassioned by these hallmarks, we strived to what would engender if an electroactive covalent organic polymer (NUF) integrated with a conductive TiO_2/TiCT (TiO_2/TiCT/NUF heterojunctions) for electrochemically detecting DA and UA (Scheme 1). The porous NUF is condensed by cyanuric chloride and melamine, where the triazine units can function as electrochemical active sites [24]; TiO_2/TiCT can adjust and optimize the interface microstructure and electron mobility. Herein, the biosensing platform has been fabricated by pipetting TiO_2/TiCT-NUF heterostructures onto carbon cloth electrodes (CCEs) (TiO_2/TiCT/NUF/CCE), where the polar functional groups derived from TiO_2/TiCT and NUF, such as –NH and –OH, can improve the interaction with the CCE surfaces, allowing the materials to more tightly adhere onto the CCE surfaces. Meanwhile, electrochemical techniques such as cyclic voltammetry (CV), electrochemical impedance spectroscopy (EIS), and differential pulse voltammetry (DPV) are utilized to evaluate the performance of different electrodes. Accordingly, the synergistic effects render TiO_2/TiCT/NUF heterostructures to produce an ultra-low LOD coupled with excellent linear range, anti-fouling property, and anti-interference ability, outperforming the previous work.

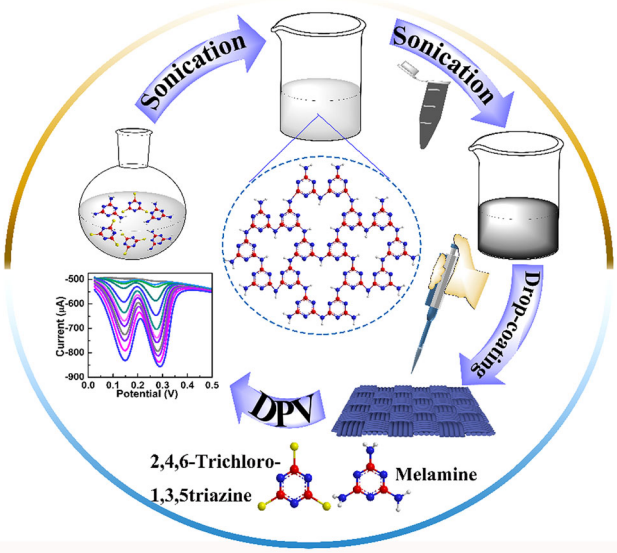

Scheme 1 Schematic representation of the fabrication process of TiO_2/TiCT/NUF/CCE

Experimental

Materials and reagents

Melamine ($C_3H_6N_6$, 99%), 2, 4, 6-Trichloro-1, 3, 5-triazine ($C_3Cl_3N_3$, 98%), and dimethyl sulfoxides (DMSO) were purchased from Macklin Biochemical Co. Ltd. Methanol (CH_3OH, 99.5%) and ethanol (CH_3CH_2OH, 99.7%) were obtained from Energy Chemical. MXene($Ti_3C_2T_X$) was purchased from Nanjing XFNANO Materials Tech Co. Ltd. The $TiO_2/Ti_3C_2T_x$ (TiO_2/TiCT) nanocomposite was obtained from the natural degradation and oxidation of Ti_3C_2 in open vials, placing MXene in air under gently stirring for 10 days at room temperature. All chemicals were analytical grade and used directly without further purification.

Preparation of the TiO_2/Ti_3C_2/NUF (TiO_2/TiCT/NUF)

2, 4, 6-Trichloro-1, 3, 5-triazine (5 mmol) and melamine (5 mmol) were dissolved in DMSO (30 mL) [24], respectively, and refluxed in a flask at 423 K for 4 days. The generated white precipitate was collected by centrifugation, and successively washed with DMSO, deionized water, and methanol for several times, and then dried at 338 K for 12 h.

The NUF suspension (1.0 g L^{-1}) was obtained by suspending NUF (10 mg) in ethanol (95%, 10 mL) under ultrasonic treatment for 2 h, and then TiO_2/TiCT (5 g L^{-1}, 0.5 mL) was added. Subsequently, the mixture was sonicated for 2 h to gain TiO_2/TiCT/NUF.

The carbon cloth electrodes (CCEs) (8 × 8 mm^2) were washed with acetone, ethanol, and deionized water, respectively, under ultrasound for 15 min. Then the CCEs were refluxed in concentrated nitric acid for 3 h at 363 K, following washed with deionized water to neutral. Subsequently, the TiO_2/TiCT/NUF dispersion (100 μL) was cast onto CCEs, and dried at 333 K for 30 min, designed as TiO_2/TiCT/NUF/CCE.

Preliminary treatment of real samples

The urine was obtained from a healthy human volunteer, and serum was purchased from KEJING Biology Co. Ltd. The urine and serum samples were first centrifuged a speed of 5000 rpm for 10 min, and then the urine and serum supernatants were diluted 500 and 100 times, respectively, using 0.1 M of phosphate buffer (PB) (pH 7.4) from sodium dihydrogen phosphate and sodium monohydrogen phosphate solutions.

Anti-fouling measurement

Fetal bovine serum (FBS) was selected to evaluate the anti-fouling capability of the electrode surface. Firstly, FBS was diluted with 0.1 M PB (pH = 7.4) to different proportions (*V*/

V). Then, the electrodes were immersed in FBS solution for 30 min. The variation of biosensing interface was monitored by electrochemical impedance spectra (EIS) in PB (0.1 M, pH = 7.4) containing 0.1 M KCl and 5 mM $[Fe(CN)_6]^{3-/4-}$.

Apparatus and measurement

The powder X-ray diffraction (PXRD) analysis was conducted on an Ultima IV X-ray diffractometer with Cu K_α (1.5418 Å) radiation under 40 kV and 30 mA. Fourier transform infrared (FT-IR) spectra were measured in the scope of 4000~400 cm^{-1} (Bruker Tensor II spectrometer) with KBr pellets. The morphology of the composites was characterized by scanning electron microscopy (SEM) (Hitachi S-4800). High-resolution transmission electron microscopy (HR-TEM) was executed on FEI TF20 microscopy. Nitrogen adsorption–desorption isotherms were gained through a TriStar II 3020 analyzer, and the samples were pretreated for 12 h at 423 K before the measurements. X-ray photoelectron spectroscopies (XPS) were recorded on an ESCALAB 250Xi spectrometer.

Cyclic voltammetry (CV), differential pulse voltammetry (DPV), and electrochemical impedance spectroscopy (EIS) measurements were performed on a PARSTAT 4000 electrochemical analyzer (Princeton Applied Research, USA). All electrochemical tests were conducted by a traditional three-electrode system, involving a platinum wire counter electrode and a saturated calomel electrode (SCE) reference electrode. The working electrode was TiO_2/TiCT/NUF-modified CCE, and CCE, NUF/CCE, TiCT/NUF/CCE, and TiO_2/NUF/CCE were adapted for comparison. The oxygen in solutions was eliminated by continuously sparging with nitrogen for at least 20 min.

Results and discussion

Choice of materials

The NUF with triazine ring has a potential for redox reaction, but is limited by the faint electrical conductivity. Thus, TiO_2/TiCT is chosen to combine with NUF for increasing the number of carriers, bringing about a good electrocatalytic ability to DA and UA for TiO_2/TiCT/NUF heterojunctions.

Structural and morphological characterization

The structure and composition of NUF, TiCT, TiO_2/TiCT, and TiO_2/TiCT/NUF are investigated by PXRD. As illustrated in Fig. 1a, the diffraction signals of anatase TiO_2 gradually strengthen, and those of TiCT appear to weakened after TiCT is partially oxidized to TiO_2; while there is no obvious pattern in the amorphous NUF ranging from 10 to 35° [24]. When TiO_2/TiCT integrated with NUF, a lower content brings about an unobvious pattern of TiCT observed in the XRD of TiO_2/TiCT/NUF. The FT-IR spectrum is also applied to monitor the

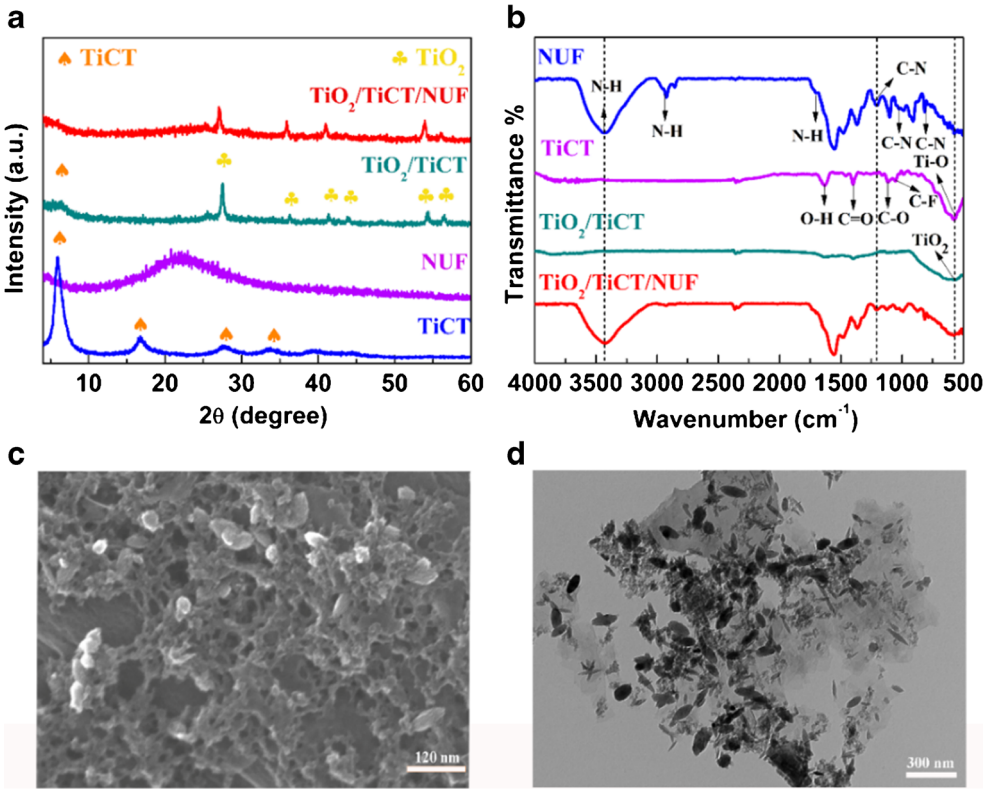

Fig. 1 **a** PXRD patterns and **b** FT-IR spectra of NUF, TiCT, TiO_2/TiCT, TiO_2/TiCT/NUF; **c** SEM and **d** TEM images of TiO_2/TiCT/NUF

groups in TiO_2/TiCT/NUF (Fig. 1b). The TiO_2/TiCT-doped NUF composite exhibits the H–N vibration at 3394, 2941, and 1705 cm^{-1}, and the C–N vibrations at 1203, 1045, and 813 cm^{-1} together with O–H (1640 cm^{-1}), C=O (1402 cm^{-1}), and wide O–Ti–O bands at 400 ~ 900 cm^{-1} [25]. These groups generate relatively strong vibration signals, despite NUF and TiCT show the weak or low crystallinity. The morphology of materials is measured by SEM and TEM. As displayed in the SEM images (Fig. S1), NUF is loose block, and TiO_2/TiCT appears as fusiform shapes with a few sheets. Furthermore, the blocky-shaped NUF particles, accompanied by fusiform TiO_2 and lamellar TiCT can be sensibly observed from the SEM and TEM images of TiO_2/TiCT/NUF (Fig. 1c, 1d), indicating the successful combination of the two materials, consistent with the PXRD results.

The N_2 absorption/desorption isotherms of the NUF and TiO_2/TiCT/NUF are displayed in Fig. S2. The N_2 uptake of NUF raises as P/P_0 increases from 0.44 to 0.9. Also, the isotherm of NUF presents an obvious hysteresis loop, belonging to a typical IV type adsorption curve, revealing the existence of mesoporous structure in NUF. The pore size of the NUF structure mainly distributes at 14.1 and 29.4 Å (Fig. S2b). Upon integrating with TiO_2/TiCT, TiO_2/TiCT/NUF has a similar adsorption curve and pore size distribution, and a relatively smaller Brunauer-Emmett-Teller surface (S_{BET} = 326.1 $m^2\ g^{-1}$) when referred to NUF (444.4 $m^2\ g^{-1}$). In accordance with SEM image, the reduction of S_{BET} is probably due to the addition of TiO_2/TiCT occupies part of the pores in NUF, small S_{BET} with large electrocatalytic activity, illustrating BET surface area is not the only factor that affects electrocatalytic performance.

X-ray photoelectron spectroscopies (XPS) is also carried out for investigating the combination of TiO_2/TiCT and NUF (Fig. 2). As monitored in Fig. 2a, the broad peak in N 1 s species (397~401 eV) from NUF is deconvoluted to three peaks at 399.4, 398.6, and 397.8 eV, respectively, corresponding to C–NH–C, dangling $–NH_2$ and C=N in the triazine ring, which also appears in TiO_2/TiCT/NUF. The TiO_2/TiCT has two pairs of Ti signals, occurring to Ti–C (459.8 and 455 eV) and TiO_2 (464.5 and 458.4 eV), respectively [26], disclosing that the TiCT has been partially oxidized to TiO_2 (Fig. 2b); meanwhile, there is a characteristic peak of Ti^{2+} (456.3 eV), possibly originating from an intermediate phase before the MXene converts to TiO_2 [27]. When TiO_2/TiCT merged with NUF, TiO_2/TiCT/NUF exhibits the similar Ti 2p signals [26], and the peak of the instable Ti^{2+} intermediate appeared weak. The TiO_2/TiCT holds the distinctive peaks in C 1 s, corresponding to C–O (286.2 eV), C–C (284.6 eV), O–C=O (288.6 eV), and C–Ti (282 eV), respectively (Fig. 2c) [28]. With respect to TiO_2/TiCT/NUF, the additional C=N (285.4 eV) and C–N (286.7 eV) are assigned to the NUF backbone, and the C–Ti signal is obviously weakened, indicating that the TiO_2/TiCT has been successfully doped into the NUF.

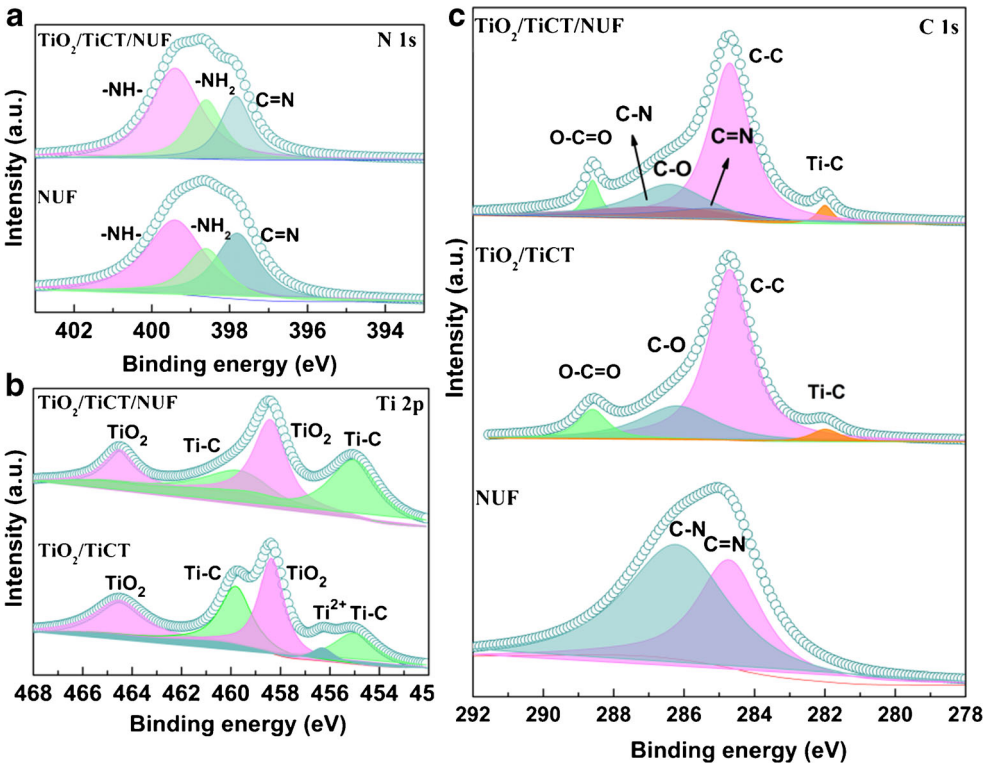

Fig. 2 XPS spectra of **a** N 1 s in TiO_2/TiCT/NUF and NUF, **b** Ti 2p in TiO_2/TiCT/NUF and TiO_2/TiCT, and **c** C 1 s in TiO_2/TiCT/NUF, TiO_2/TiCT, and NUF

Electrochemical behaviors of modified CCEs

Electrochemical behavior of TiO_2/TiCT/NUF/CCE electrode

Electrochemically active surface area (SA) is calculated by recording CV response of $[Fe(CN)_6]^{3-/4-}$ (0.5 mM) with various scan rates (υ, 20 to 300 mV s^{-1}). As observed in Fig. S3, the currents of anodic and cathodic peaks and peak-to-peak potential distance gradually enlarge with an increase of scanning rate at all modified electrodes, illustrating quasi-reversible electron-transfer behavior. Further, the I_{pa}/I_{pc} ratio lies in the range of 1.10~1.17 confirms the quasi-reversible behavior [29]. The SA is determined using the Randles–Sevcik equation (Eqs. (1)).

$$I_p = 269n^{3/2}AD^{1/2}\upsilon^{1/2}c \quad (1)$$

where I_p is the peak current, $A(cm^2)$ is the effective area of the modified electrode, D is the diffusion coefficient and C(mol dm^{-3}) is the concentration of the redox probe $[Fe(CN)_6]^{3-/4-}$ undergoing one-electron transfer reaction ($n = 1$). The SA for CCE, NUF/CCE, TiCT/NUF/CCE, TiO_2/NUF/CCE, and TiO_2/TiCT/NUF/CCE is estimated to be 0.81, 4.69, 13.34, 10.62, and 21.65 cm^2, respectively (Fig. S3a-S3i). Therefore, the existence of TiO_2/TiCT immensely enhances the SA of the TiO_2/TiCT/NUF-modified CCE.

We analyzed the electrochemical properties of the electrodes measured by cyclic voltammetry (CV) at a fixed scan rate of 50 mV s^{-1} and electrochemical impedance spectroscopy (EIS) under 0.1 M KCl solution containing 5 mM $[Fe(CN)_6]^{3-/4-}$ probe. As displayed in Fig. 3a, the redox peak current of the TiO_2/TiCT/NUF-modified CCE towards $[Fe(CN)_6]^{3-/4-}$ probe is 1.4-, 1.5-, 13.2-, and 270-fold higher than those of TiO_2/NUF/CCE, TiCT/NUF/CCE, NUF/CCE, and CCE, respectively; its CV area is the largest, illustrating excellent electrocatalytic activity. Regarding the EIS in Fig. 3b, the semicircle diameter of the Nyquist plot from CCE is magnified up to 29.9 Ω (R_{ct}) than that of the NUF/CCE (22.7 Ω), TiCT/NUF/CCE (20.65 Ω), TiO_2/NUF/CCE (17.89 Ω), indicating elevated charge transfer kinetics on the material modified electrodes. Besides, TiO_2/TiCT/NUF/CCE shows minimal R_{ct} (15.66 Ω), ascribed to the improved conductivity. The large electrode effective area, catalytic ability, superior conductivity, and charge transfer ability could accelerate electron transfer capability and have potential as sensing platform.

Electrocatalytic properties of TiO_2/TiCT/NUF/CCE

CVs are recorded in the absence and presence of DA (10 μM) and UA (10 μM) in PB (pH 7.4) at the bare CCE, NUF/CCE, TiCT/NUF/CCE, TiO_2/NUF/CCE, and TiO_2/TiCT/NUF/

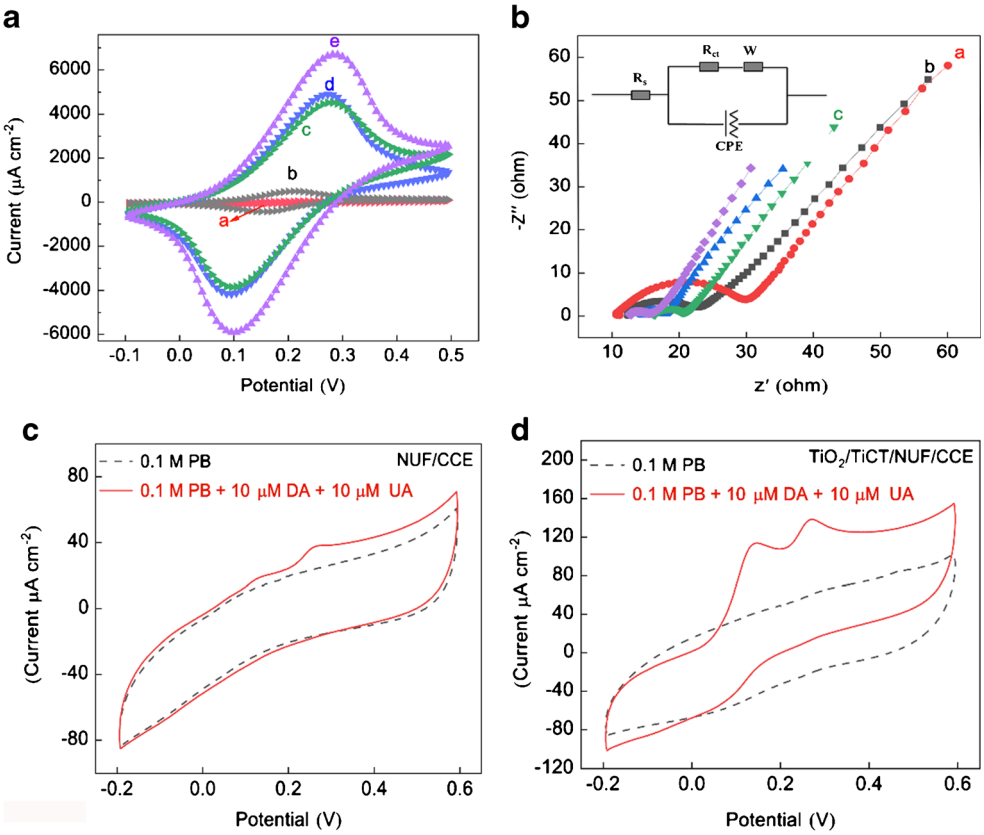

Fig. 3 **a** CVs recorded at scan rate of 50 mV s^{-1} and **b** Nyquist diagrams of different electrodes in 0.1 M KCl solution containing 5 mM $Fe(CN)_6^{3-/4-}$; CV curves of NUF/CCE (**c**) and TiO_2/TiCT/NUF/CCE (**d**) in the absence and presence of DA (10 μM) and UA (10 μM) in 0.1 M PB solution (pH 7.4). The different curves represent (a) CCE; (b) NUF/CCE; (c) TiCT/NUF/CCE; (d) TiO_2/NUF/CCE; and (e) TiO_2/TiCT/NUF/CCE, respectively

CCE under the scan rate of 50 mV s^{-1} (Fig. 3 and S4). There is no discernible oxidation response in all electrodes without DA and UA. Under the potential range of − 0.6~0.2 V (versus SCE), the decomposition of the water brings about the sharply elevated current of TiCT/NUF/CCE in PB solution (Fig. S4b). However, a lower amount of TiCT in TiO_2/TiCT/NUF/CCE fails to rouse the oxygen evolution (Fig. 3d) [30]. After DA and UA addition, the oxidation peaks towards DA and UA occur on the modified CCE electrodes. As depicted in Fig. 3c, the associated peaks linking to the oxidation of DA (0.144 V versus SCE) and UA (0.275 V versus SCE) exist in NUF/CCE due to the catalytic activity of NUF towards DA and UA. Contrasted with those of TiCT/NUF/CCE and TiO_2/NUF/CCE (Fig. S4), the largest current intensity figures in the detection curves of DA and UA on TiO_2/TiCT/NUF/CCE.

Influence on pH and electrochemical kinetics

The CV current responses of UA and DA at TiO_2/TiCT/NUF/CCE depend upon the pH of buffer medium (pH 5.0~9.0). As presented in Fig. S5, the E_{pa} values of DA and UA stick out an opposite direction as the pH of PB magnifies. The linear relationship of E_{pa} versus pH is accorded with the following equation:

$$E_{pa}(V) = -0.065\text{pH} + 0.62 \quad (R^2 = 0.994) \tag{2}$$

$$E_{pa}(V) = -0.069\text{pH} + 0.82 \quad (R^2 = 0.992) \tag{3}$$

The derived slopes border on the theoretical value figured from the Nernst eq. (0.0598 V pH^{-1}), demonstrating that the number of the electron and proton associated with electrode reaction is equal [31]. Besides, it can be discovered that the larger anodic current of TiO_2/TiCT/NUF/CCE towards DA and UA is located at pH 6 and 5, respectively. While, we chose a pH 7.4 PB as suitable electrolyte for further experiments, proceeding from feasibility and practicability.

The reaction kinetics of DA (10 μM) and UA (20 μM) at TiO_2/TiCT/NUF/CCE is also contemplated by CV measurements, and the effect of scan rate (υ) on peak current (I_p) and peak potential (E_p) in PB (0.1 M, pH 7.4) are presented in Fig. S6. The positive shift in I_p of DA (I_{DA}) and UA (I_{UA}) depends on the square root of scan rate ($\upsilon^{1/2}$, 20 to 200 mV s^{-1}). The good linear correlation generates between I_p versus $\upsilon^{1/2}$, illustrating that the oxidation of DA and UA (Eqs. (4) and (5)) at TiO_2/TiCT/NUF/CCE are regulated by a typical diffusion-controlled process. [32]

$$I_{DA}\ (\mu A) = 384.92\ \upsilon^{1/2}\left(V\ s^{-1}\right)^{1/2} - 44.8 \quad \left(R^2 = 0.997\right) \tag{4}$$

$$I_{UA}(\mu A) = 506.49\ \upsilon^{1/2}\left(V\ s^{-1}\right)^{1/2} - 45.8 \quad \left(R^2 = 0.997\right) \tag{5}$$

Moreover, an irreversible reaction can be described by Laviron's equation (Eqs. (6)):

$$E_p = E^0 - \frac{2.3RT}{n\alpha F}\log\frac{RTK_s}{n\alpha F} + \frac{2.3RT}{n\alpha F}\log\upsilon \tag{6}$$

where E^0 is the formal potential (V), n is the number of transferred electrons, α is the charge-transfer coefficient, K_s is the standard heterogeneous electron transfer rate constant and other parameters represent conventional meanings. Accordingly, oxidation peak potentials (E_p) of DA and UA (Eqs. (7) and (8)) as function of the logarithm of scan rates (log υ) are plotted in Fig. S6:

$$E_{DA}(V) = 0.050\ \log\upsilon\left(V\ s^{-1}\right) + 0.19 \quad \left(R^2 = 0.995\right) \tag{7}$$

$$E_{UA}(V) = 0.052\ \log\upsilon\left(V\ s^{-1}\right) + 0.33 \quad \left(R^2 = 0.998\right) \tag{8}$$

According to the slopes of E_p – log(υ) curves (2.303RT/αnF), the αn value is 1.18 (DA) and 1.13 (UA), respectively. Also, the linear equation (Eqs. (9)) is adopted to estimate n (approximately 2) [33], where D is assumed to be 6.2×10^{-6} (DA) [34] and 2.75×10^{-6} cm^2 s^{-1} (UA). [3] The calculated results vote two electrons transfer processes of electrocatalytic reactions emerged at the TiO_2/TiCT/NUF/CCE electrode. Then, K_s value of 0.92 and 1.1 s^{-1} is obtained for TiO_2/TiCT/NUF/CCE towards DA and UA oxidation, respectively (Eqs. (6)).

$$I_p = \left(0.4958 \times 10^{-3}\right)nF^{3/2}(RT)^{-1/2}(\alpha n)^{1/2}AcD^{1/2}\upsilon^{1/2} \tag{9}$$

Based on the relationship between E_{pa} and pH, the number of electrons and protons involved in the reaction is equal, and thus, it can be speculated that two electrons and two protons involve in the DA and UA oxidation. The mechanism is described as follows:

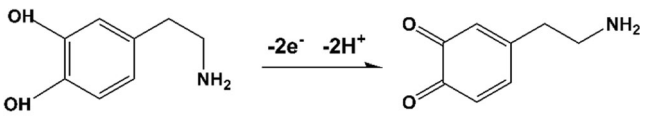

Dopamine oxidation

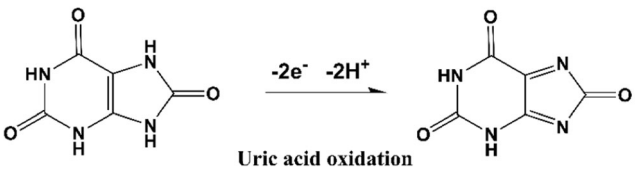

Uric acid oxidation

The triazine units redox-activated in the NUF can function as electrochemical active sites, and the blend of conductive TiO_2/TiCT would increase the number of carriers, and further employ abundant electrons to involve into the reaction, which could improve the conductivity of TiO_2/TiCT/NUF composite. The heterojunctions formed in TiO_2, TiCT, and NUF make the composite possess large effective active area, and

optimized electron transfer capability, which is beneficial to the oxidation of DA and UA.

Simultaneous determination of DA and UA

The differential pulse voltammetry (DPV) technique is harnessed to appraise the determination of DA and UA using TiO_2/TiCT/NUF/CCE. Figure 4 depicts the DPV curves of TiO_2/TiCT/NUF/CCE towards DA (0.002 to 100 μM) and UA (0.001 to 120 μM) under the optimized conditions. The peak current of TiO_2/TiCT/NUF/CCE steadily increases with an increase of detected compound concentrations (C_{DA} and C_{UA}), respectively. Similarly, the linear and exponential fittings of C_{DA} (Eqs. (10) and (11)) and C_{UA} (Eqs. (12) and (13)) versus the current response can be obtained over low and high concentration regions, respectively, as stated in the function below:

$$I_p(\mathrm{DA}) = 7.69C_{DA} + 3.27 \quad (R^2 = 0.998) \tag{10}$$

$$I_p(\mathrm{DA}) = 250.31\left(1-0.96^{C_{DA}}\right) \quad (R^2 = 0.995) \tag{11}$$

$$I_p(\mathrm{UA}) = 8.58C_{UA} + 12.33 \quad (R^2 = 0.991) \tag{12}$$

$$I_p(\mathrm{UA}) = 449.64-574.49 \times 0.96^{C_{UA}} \quad (R^2 = 0.994) \tag{13}$$

Figure 5 illustrates the DPV curves that C_{UA} (1.0 to 10.0 μM) and C_{DA} (4.0 to 13.0 μM) accompanying by DA (15.0 μM) and UA (10 μM) for simultaneous detection, respectively, indicating that there is little effect on the determination of UA in the presence of DA. The I_{pa} is proportional to C_{UA} and C_{DA}, following the linear equations ((Eqs. (14)) and (15)):

$$I_p(\mu\mathrm{A}) = 8.2C_{UA} + 17.66 \left(R^2 = 0.997\right) \tag{14}$$

$$I_p(\mu\mathrm{A}) = 7.44C_{DA} + 12.58\left(R^2 = 0.999\right) \tag{15}$$

Additionally, the simultaneous detections of DA and UA are also performed by DPV technique (Fig. 5e). As seen, DPV curves reflect two well-separated anodic peaks, pertaining to the oxidation of DA (E_{pa} = 0.144 V) and UA (E_{pa} = 0.275 V) on the TiO_2/TiCT/NUF/CCE, respectively. The synchronous additions of DA (0.002~100 μM) and UA (0.001~60 μM) unfold a variation in I_{pa} versus concentrations. According to the signal-to-noise (S/N = 3), the limit of detection (LOD) is estimated to be 0.2 nM (DA) and 0.18 nM (UA), with the sensitivity of 9.2× 10^{-3} and 8.3 × 10^{-3} μA nM^{-1} cm^{-2}, respectively. The results testify that the TiO_2/TiCT/NUF/CCE biosensor can cooperatively detect DA and UA, with no noticeable interference from each other. It can be noted that the proposed biosensor has a better performance for the detection of DA and UA particularly over that of other sensors in terms of limit of detection and detection range (Table S1). Meanwhile, we also compared the proposed electrochemical sensor with other previous methods (Table S2), the detection limit of which is superior to fluorometry and colorimetry.

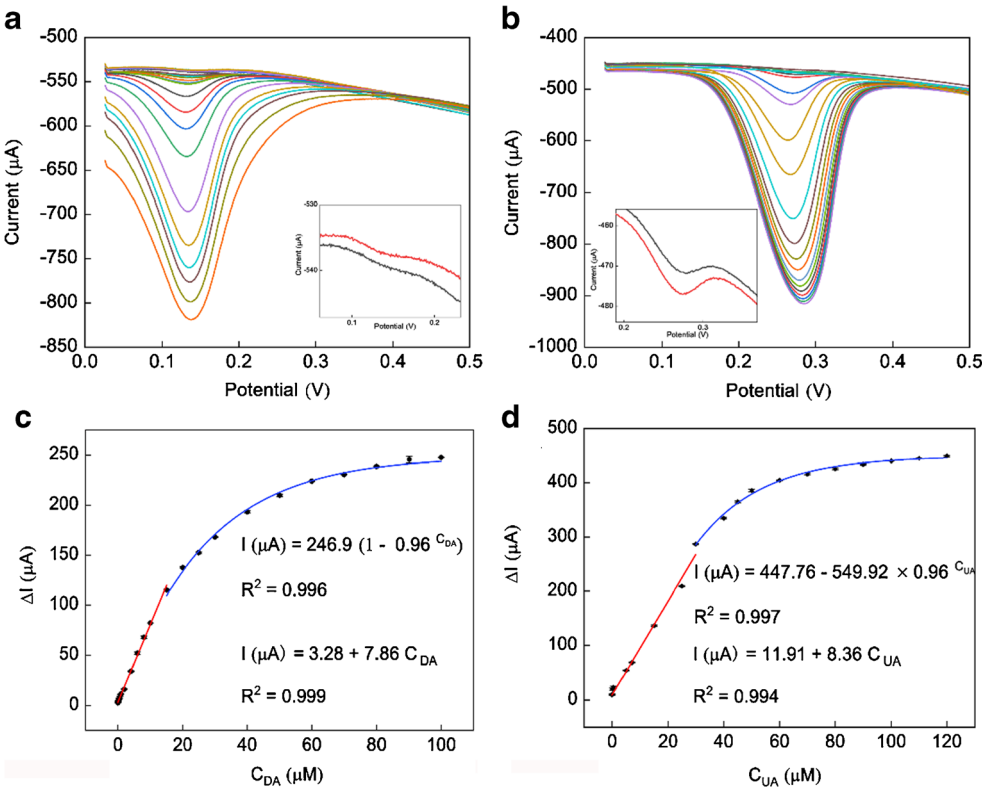

Fig. 4 DPVs of TiO_2/TiCT/NUF/CCE applied at the potential range of 0.0 to 0.5 V in 0.1 M PB solution (pH 7.4) with various concentrations of **a** DA (0.002~100 μM) (Illustration is 0.002~0.02 μM) and **b** UA (0.001~120 μM) (Illustration is 0.001~0.01 μM); the corresponding plots of **c** I_{pa} vs C_{DA}, SD (± 0.64, n = 3) and **d** I_{pa} vs C_{UA}, SD (± 1.2, n = 3)

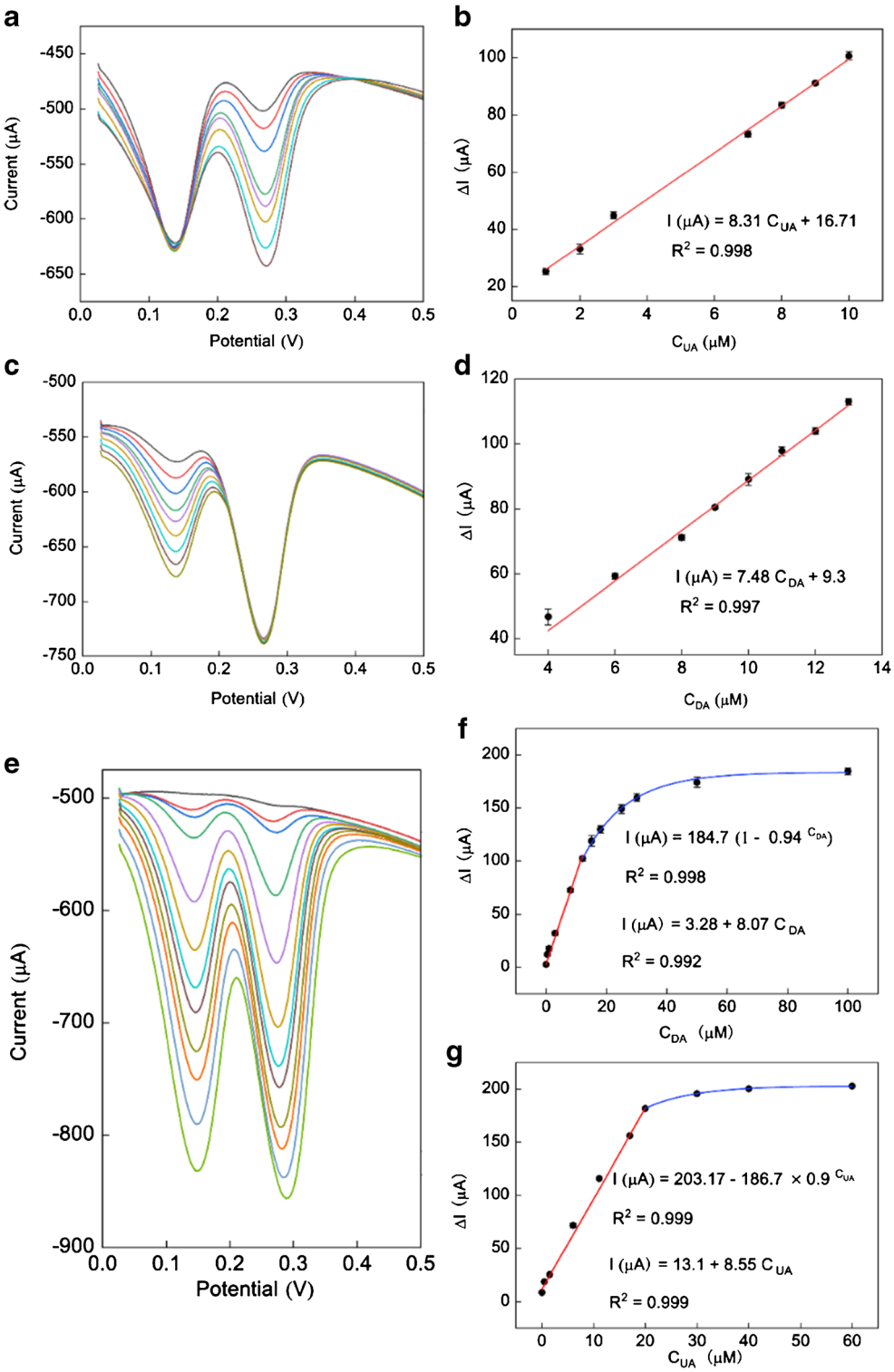

Fig. 5 DPV profiles of TiO_2/TiCT/NUF/CCE in 0.1 M PB (pH 7.4) containing **a** 15 μM DA with 1.0~10.0 μM of UA, **c** 10 μM UA with 4.0~13 μM of DA, and **e** 0.002~100 μM of DA and 0.001~60 μM of UA; the corresponding linear plots of I_p vs concentration towards the sole UA **b** (SD (± 1.13)), the sole DA **d** (SD (± 1.24)), and the mixture of DA **f** (SD (± 2.88)) and UA **g** (SD (± 0.61))

Repeatability, reproducibility, and stability

Repeatability, reproducibility, and stability are important parameters to evaluate the performance of biosensor. The TiO_2/TiCT/NUF/CCE is continuously measured the response of DA (5.0 μM) and UA (5.0 μM) for five successive measurements; the relative standard derivation (RSDs, $n = 5$) for DA and UA is 1.4% and 0.42%, respectively (Fig. S7). The reproducibility of the sensor is obtained by using five modified electrodes, and the calculated RSD is 0.69% for DA and 0.89% for UA (Figure S7). The stability of TiO_2/TiCT/NUF/CCE is evaluated after exposing the electrode into

the refrigerator at 277 K, where the response remains *ca.* 98.5% and 97.0% for DA and UA, respectively, after 4 days (Fig. S8). Besides, as illustrated in SEM imagines (Fig. S9), the TiO_2/TiCT/NUF is still retained on the CCE surface after electrochemical measurement, testifying its robustness on CCE surface. These results verify that the fabricated biosensor has excellent reversibility, repeatability, reproducibility, and stability for the electrochemical detection of DA and UA.

Interference and antifouling property

The anti-interference performance is a critical property indicator for nonenzymatic biosensor. Some possible interferences coexist with DA and UA in real samples. Figure 6 shows the current responses of DA (20 μM) and UA (10 μM) in the presence of 10-fold interferes including inorganic salt ions (NaCl) and bioactive molecules (urea, glucose, glycine, H_2O_2, folic acid, and ascorbic acid). The interferences of these possible coexisting substances are calculated by the selectivity coefficient (k_{sel}) (Eqs. (16)). In any case, the k_{sel} values are inferior to 0.07, illustrating excellent selectivity of TiO_2/TiCT/NUF/CCE. Furthermore, for ascorbic acid (AA) likely to affect the electrochemical detection of DA and UA, additional CV and DPV measurements are carried out for the simultaneous detection of AA, DA, and UA. As shown in Fig. S10, there is no marked redox peak of AA either in single AA or in the three mixtures. Furthermore, the high concentration of AA observably no interferes with the detection of DA and UA, and displays in Fig. S11.

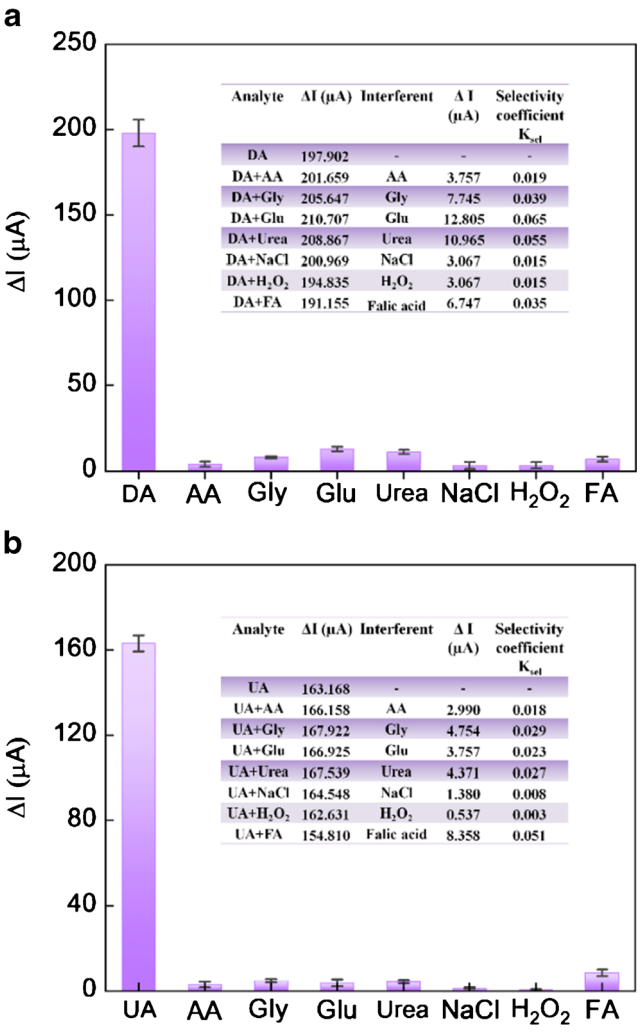

Fig. 6 The graphs of DPV current responses of TiO_2/TiCT/NUF/CCE towards DA (20 μM) and UA (10 μM) in the presence of 10-fold coexisting substances: ascorbic acid (AA), glycine (Gly), glucose (Glu), urea, NaCl, H_2O_2, and folic acid (FA)

$$k_{sel} = (\text{Signal})_{\text{interferent}}/(\text{Signal})_{\text{analyte}} \quad (16)$$

In complex biological samples, the presence of non-specific protein would affect the practical application of electrodes [35]. Here, electrochemical impedance spectroscopy (EIS) is performed to monitor the interface variation of the electrode with and without incubating in different dilution ratios (*V*/*V*) of FBS solution. As shown in Fig. S12, there is no significant change in the EIS signal (R_{et}) when the FBS concentration is below 10%. The R_{et} shows the 7.3% and 40% increases after immersing in 20% and 100% FBS, respectively, indicating that the proposed biosensor shows considerable anti-fouling ability.

Analysis of real samples

The applicability of the developed biosensor in real samples is evaluated by measuring DA and UA in urine and serum (10 mL) by DPV analysis (Fig. S13 and S14). The known DA and UA concentrations are added to the diluted samples (supporting information). As displayed in Table 1, the satisfactory recoveries of the spiked samples for DA and UA ranging from 98.4 to 100.9%, with RSD values below 1.0%. These analytical results demonstrate that TiO_2/TiCT/NUF/CCE has great practicability and validity for the routine analysis of DA and UA in real samples.

Table 1 Recoveries of DA and UA using TiO_2/TiCT/NUF/CCE in urine and serum samples

Sample	Analytes	Determined (μM)	Added (μM)	Found (μM)	Recovery (%)
Urine	DA	5.7	5.0	10.72	100.2
			7.0	12.70	100.0
	UA	6.7	1.0	7.74	100.5
			5.0	11.80	100.9
Serum	DA	0.3	2.0	2.30	100.0
			5.0	5.30	100.0
	UA	3.4	3.0	6.30	98.4
			13.0	16.25	99.1

Conclusion

In this study, a novel biomimetic non-enzyme sensor for simultaneous detection of dopamine (DA) and uric acid (UA) is constructed based on covalent organic polymer (NUF) and $TiO_2/Ti_3C_2T_x$ (TiO_2/TiCT), which can effectively solve the problems of low electroconductivity of NUF and weak biocatalysis activity of $Ti_3C_2T_x$. Due to the advantages of abundant redox sites, large electroactive area, and enhanced electron transfer capacity along with heterostructures, wide linear ranges and ultra-low detection limits for simultaneous measurement of DA and UA are reflected. Furthermore, TiO_2/TiCT/NUF/CCE is not only immune to co-existing interference under the presence of 10-fold glycine, glucose, urea, NaCl, H_2O_2, and folic acid along with 25-fold ascorbic acid, but also directly applicable to determine DA and UA concentrations in urine and serum samples with satisfactory results. Moreover, the proposed biosensor could effectively prevent the non-specific adsorption of protein on the electrode surface. Predominantly, the TiO_2/TiCT/NUF can validate a candidate of biosensor for active biomolecules in medical diagnosis and food supervision.

Supplementary Information The online version contains supplementary material available at https://doi.org/10.1007/s00604-021-04755-8.

Funding This study received financial support from the National Natural Science Foundation of China (Nos. 21771047, 21403048, 21401147 and 21571045), University Nursing Program for Young Scholars with Creative Talents in Heilongjiang Province (No. UNPYSCT-2017183), Harbin Science and Technology Bureau (2016RAQXJ161), and PhD Research Startup Program of Harbin Normal University, China (No. XKB201310).

Declarations

Competing interests The authors declare no competing interests.

Conflict of interest The authors declare that they have no competing of interests.

Supplementary Information The online version contains supplementary material available at https://doi.org/10.1007/s00604-021-04755-8.

References

1. Zhang W, Liu L, Li Y, Wang D, Ma H, Ren H, Shi Y, Han Y, Ye BC (2018) Electrochemical sensing platform based on the biomass-derived microporous carbons for simultaneous determination of ascorbic acid, dopamine, and uric acid. Biosens Bioelectron 121: 96–103
2. Lu D, Fan M, Cai R, Huang Z, You R, Huang L, Feng S, Lu Y (2020) Silver nanocube coupling with a nanoporous silver film for dual-molecule recognition based ultrasensitive SERS detection of dopamine. Analyst 145(8):3009–3016
3. Shahamirifard SA, Ghaedi M, Razmi Z, Hajati S (2018) A simple ultrasensitive electrochemical sensor for simultaneous determination of gallic acid and uric acid in human urine and fruit juices based on zirconia-choline chloride-gold nanoparticles-modified carbon paste electrode. Biosens Bioelectron 114:30–36
4. Li N, Nan C, Mei X, Sun Y, Feng H, Li Y (2020) Electrochemical sensor based on dual-template molecularly imprinted polymer and nanoporous gold leaf modified electrode for simultaneous determination of dopamine and uric acid. Mikrochim Acta 187(9):496
5. Zhang X, Chen X, Kai S, Wang HY, Yang J, Wu FG, Chen Z (2015) Highly sensitive and selective detection of dopamine using one-pot synthesized highly photoluminescent silicon nanoparticles. Anal Chem 87(6):3360–3365
6. Liu Y, Li H, Guo B, Wei L, Chen B, Zhang Y (2017) Gold nanoclusters as switch-off fluorescent probe for detection of uric acid based on the inner filter effect of hydrogen peroxide-mediated enlargement of gold nanoparticles. Biosens Bioelectron 91:734–740
7. Amjadi M, Hallaj T, Nasirloo E (2020) In situ formation of Ag/Au nanorods as a platform to design a non-aggregation colorimetric assay for uric acid detection in biological fluids. Microchem J 154:104642
8. Yu L, Butler D, Lucking MC, Zhang F, Xia T, Fujisawa K, Nakajima TG, Silva RC, Endo M, Terrones M, Terrones M, Ebrahimi A (2020) Single-atom doping of MoS_2 with manganese enables ultrasensitive detection of dopamine: experimental and computational approach. Sci Adv 6:eabc4250
9. Sajid M, Nazal MK, Mansha M, Alsharaa A, Jillani SMS, Basheer C (2016) Chemically modified electrodes for electrochemical detection of dopamine in the presence of uric acid and ascorbic acid: a review. TrAC Trends Anal Chem 76:15–29
10. Iranmanesh T, Foroughi MM, Jahani S, Shahidi Zandi M, Hassani Nadiki H (2020) Green and facile microwave solvent-free synthesis of CeO_2 nanoparticle-decorated CNTs as a quadruplet electrochemical platform for ultrasensitive and simultaneous detection of ascorbic acid, dopamine, uric acid and acetaminophen. Talanta 207: 120318
11. Li YY, Kang P, Wang SQ, Liu ZG, Li YX, Guo Z (2021) Ag nanoparticles anchored onto porous CuO nanobelts for the ultrasensitive electrochemical detection of dopamine in human serum. Sensors Actuators B Chem 327:128878
12. Wang M, Hu M, Liu J, Guo C, Peng D, Jia Q, He L, Zhang Z, Du M (2019) Covalent organic framework-based electrochemical aptasensors for the ultrasensitive detection of antibiotics. Biosens Bioelectron 132:8–16
13. Cao X, Xu H, Dong S, Xu J, Qiao Z, Zhao S, Wang J, Wang Z (2020) Preparation of high-performance and pressure-resistant mixed matrix membranes for CO_2/H_2 separation by modifying COF surfaces with the groups or segments of the polymer matrix. J Membr Sci 601:117882
14. Li CC, Gao MY, Sun XJ, Tang HL, Dong H, Zhang FM (2020) Rational combination of covalent-organic framework and nano TiO_2 by covalent bonds to realize dramatically enhanced photocatalytic activity. Appl Catal B 266:118586
15. Cui X, Lei S, Wang AC, Gao L, Zhang Q, Yang Y, Lin Z (2020) Emerging covalent organic frameworks tailored materials for electrocatalysis. Nano Energy 70:104525
16. Wang J, Yang X, Wei T, Bao J, Zhu Q, Dai Z (2018) Fe-Porphyrin-based covalent organic framework as a novel peroxidase mimic for a one-pot glucose colorimetric assay. ACS Appl Bio Mater 1(2): 382–388
17. Zhang D, Wang Y, Geng W, Liu H (2019) Rapid detection of tryptamine by optosensor with molecularly imprinted polymers based on carbon dots-embedded covalent-organic frameworks. Sensors Actuators B Chem 285:546–552

18. Zhang X, Li G, Wu D, Zhang B, Hu N, Wang H, Liu J, Wu Y (2019) Recent advances in the construction of functionalized covalent organic frameworks and their applications to sensing. Biosens Bioelectron 145:111699
19. Sun Y, He J, Waterhouse GIN, Xu L, Zhang H, Qiao X, Xu Z (2019) A selective molecularly imprinted electrochemical sensor with GO@COF signal amplification for the simultaneous determination of sulfadiazine and acetaminophen. Sensors Actuators B Chem 300:126993
20. Liang C, Lin H, Wang Q, Shi E, Zhou S, Zhang F, Qu F, Zhu G (2020) A redox-active covalent organic framework for the efficient detection and removal of hydrazine. J Hazard Mater 381:120983
21. Zhao L, Dong B, Li S, Zhou L, Lai L, Wang Z, Zhao S, Han M, Gao K, Lu M, Xie X, Chen B, Liu Z, Wang X, Zhang H, Li H, Liu J, Zhang H, Huang X, Huang W (2017) Interdiffusion reaction-assisted hybridization of two-dimensional metal-organic frameworks and Ti_3C_2Tx nanosheets for electrocatalytic oxygen evolution. ACS Nano 11(6):5800–5807
22. Xu Y, Wang S, Yang J, Han B, Nie R, Wang J, Wang J, Jing H (2018) In-situ grown nanocrystal TiO_2 on 2D Ti_3C_2 nanosheets for artificial photosynthesis of chemical fuels. Nano Energy 51:442–450
23. Li N, Jiang Y, Zhou C, Xiao Y, Meng B, Wang Z, Huang D, Xing C, Peng Z (2019) High-performance humidity sensor based on urchin-like composite of Ti_3C_2 MXene-derived TiO_2 nanowires. ACS Appl Mater Interfaces 11(41):38116–38125
24. Xue R, Guo H, Yue L, Wang T, Wang M, Li Q, Liu H, Yang W (2018) Preparation and energy storage application of a long-life and high rate performance pseudocapacitive COF material linked with –NH–bonds. New J Chem 42(16):13726–13731
25. Zhang S, Zhao X, Li B, Bai C, Li Y, Wang L, Wen R, Zhang M, Ma L, Li S (2016) "Stereoscopic" 2D super-microporous phosphazene-based covalent organic framework: design, synthesis and selective sorption towards uranium at high acidic condition. J Hazard Mater 314:95–104
26. Li Q, Zhong B, Zhang W, Jia Z, Jia D, Qin S, Wang J, Razal JM, Wang X (2019) Ti_3C_2 MXene as a new nanofiller for robust and conductive elastomer composites. Nanoscale 11(31):14712–14719
27. Zhang CJ, Pinilla S, McEvoy N, Cullen CP, Anasori B, Long E, Park SH, Seral Ascaso A, Shmeliov A, Krishnan D, Morant C, Liu X, Duesberg GS, Gogotsi Y, Nicolosi V (2017) Oxidation stability of colloidal two-dimensional titanium carbides (MXenes). Chem Mater 29(11):4848–4856
28. Chen Y, Wang D, Lin Y, Zou X, Xie T (2019) In suit growth of CuSe nanoparticles on MXene (Ti_3C_2) nanosheets as an efficient counter electrode for quantum dot-sensitized solar cells. Electrochim Acta 316:248–256
29. Verma S, Arya P, Singh A, Kaswan J, Shukla A, Kushwaha HR, Gupta S, Singh SP (2020) ZnO-rGO nanocomposite based bioelectrode for sensitive and ultrafast detection of dopamine in human serum. Biosens Bioelectron 165:112347
30. Wang Y, Wu Q, Zhang B, Tian L, Li K, Zhang X (2020) Recent advances in transition metal carbide electrocatalysts for oxygen evolution reaction. Catalysts 10(10):1164
31. Raj M, Gupta P, Goyal RN, Shim YB (2017) Graphene/conducting polymer nano-composite loaded screen printed carbon sensor for simultaneous determination of dopamine and 5-hydroxytryptamine. Sensors Actuators B Chem 239:993–1002
32. Huang Q, Zhang H, Hu S, Li F, Weng W, Chen J, Wang Q, He Y, Zhang W, Bao X (2014) A sensitive and reliable dopamine biosensor was developed based on the au@carbon dots-chitosan composite film. Biosens Bioelectron 52:277–280
33. Liang Z, Zhai H, Chen Z, Wang H, Wang S, Zhou Q, Huang X (2016) A simple, ultrasensitive sensor for gallic acid and uric acid based on gold microclusters/sulfonate functionalized graphene modified glassy carbon electrode. Sensors Actuators B Chem 224:915–925
34. Yan X, Gu Y, Li C, Tang L, Zheng B, Li Y, Zhang Z, Yang M (2016) Synergetic catalysis based on the proline tailed metalloporphyrin with graphene sheet as efficient mimetic enzyme for ultrasensitive electrochemical detection of dopamine. Biosens Bioelectron 77:1032–1038
35. Wang S, Ma Y, Wang Y, Jiao M, Luo X, Cui M (2020) One-step electrodeposition of poly(m-aminobenzoic acid) membrane decorated with peptide for antifouling biosensing of Immunoglobulin E. Colloids Surf B: Biointerfaces 186:110706